



SPE 59286

Transient Foam Flow in Homogeneous Porous Media: Surfactant Concentration and Capillary End Effects

O.G. Apaydin*, SPE and A.R. Kovscek, SPE, Stanford University

Copyright 2000, Society of Petroleum Engineers Inc.

This paper was prepared for presentation at the 2000 SPE/DOE Improved Oil Recovery Symposium held in Tulsa, Oklahoma, 3–5 April 2000.

This paper was selected for presentation by an SPE Program Committee following review of information contained in an abstract submitted by the author(s). Contents of the paper, as presented, have not been reviewed by the Society of Petroleum Engineers and are subject to correction by the author(s). The material, as presented, does not necessarily reflect any position of the Society of Petroleum Engineers, its officers, or members. Papers presented at SPE meetings are subject to publication review by Editorial Committees of the Society of Petroleum Engineers. Electronic reproduction, distribution, or storage of any part of this paper for commercial purposes without the written consent of the Society of Petroleum Engineers is prohibited. Permission to reproduce in print is restricted to an abstract of not more than 300 words; illustrations may not be copied. The abstract must contain conspicuous acknowledgment of where and by whom the paper was presented. Write Librarian, SPE, P.O. Box 833836, Richardson, TX 75083-3836, U.S.A., fax 01-972-952-9435.

Abstract

Foaming injected gas is a useful and promising technique for achieving mobility control in porous media. Typically, such foams are aqueous. In the presence of foam, gas and liquid flow behavior is determined by bubble size or foam texture. The thin-liquid films that separate foam into bubbles must be relatively stable for a foam to be finely textured and thereby be effective as a displacing or blocking agent. Film stability is a strong function of surfactant concentration and type. This work studies foam flow behavior at a variety of surfactant concentrations using experiments and a numerical model. Thus, the foam behavior examined spans from strong to weak.

Specifically, a suite of foam displacements over a range of surfactant concentrations were monitored in a roughly 7 μm^2 , one-dimensional sandpack using X-ray computed tomography (CT). Sequential pressure taps were employed to measure flow resistance. Nitrogen was the gas and an alpha olefin sulfonate (AOS 1416) in brine was the foamer. Surfactant concentrations studied varied from 0.005 to 1 wt%. Because foam mobility depends strongly upon its texture, a bubble population balance model is both useful and necessary to describe the experimental results thoroughly and self consistently. Excellent agreement is found between experiment and theory.

Introduction

Foam is suggested by many investigators to improve the

sweep efficiency of multi-phase displacement processes. Aqueous foams are most common and are formed by dispersing non-wetting gases within a continuous surfactant-laden liquid phase either by alternating or co-injection of gas and surfactant solution into porous media. For example, surfactant soil flushing is recommended for aquifer remediation of dense organic liquids¹. However, flushing is difficult where there are low permeability regions and depressions in the aquifer that permit the dense organic phase to accumulate. Injecting gas with the surfactant solution to generate a foam in situ enhances sweep and improves remediation^{2,3}.

In enhanced oil recovery (EOR) gases such as steam, carbon dioxide, enriched hydrocarbons, and nitrogen are injected into oil reservoirs to improve recovery. These gases are usually less viscous than water, and oil and they often channel selectively through high permeability zones or rise to the top of the reservoir by gravity segregation. As a result, sweep efficiency decreases and the amount of oil left behind increases. Again, foaming the gas might overcome the mobility problem of gas-drive fluids and improve the contact with the oil because foam encounters large flow resistance in porous media⁴⁻⁶.

Despite the varied field applications, foam behavior in porous media is far from understood. This work probes experimentally the effect of surfactant concentration on foam flow in homogeneous porous media and demonstrates a model to predict accurately the generation, coalescence, and transport of foam. To this end, experiments in a homogeneous sand with a commercial surfactant at a variety of surfactant concentrations have been conducted. We hope to provide a description of foam that begins to address the variable surfactant concentration conditions.

The progress of foam displacement at low injection rates is monitored with X-ray computed tomography (CT) and measurement of pressure profiles. Some experiments exhibit end effects that are well described by application of the model under local equilibrium conditions. Even at low surfactant concentrations, a significant effect of foam on displacement efficiency is witnessed.

Interaction of foam with oil is not included here to avoid confusing foam-oil effects with foam coalescence. However,

* currently at Holditch-Reservoir Technologies

foam-oil interactions are discussed elsewhere including their incorporation into a mechanistic simulation framework^{7,8}. Likewise, experiments regarding foam generation and propagation in multidimensional heterogeneous porous media have also been conducted⁹. Before discussing the experimental setup, results, simulation of the experiments, and the interpretation of end effects on foam flow, it is helpful to review gas-mobility reduction mechanisms and the role of surfactant in foam displacement.

Gas Mobility Reduction

Foam alters gas mobility in two ways. The first mechanism is associated with moving bubbles and rearrangement of bubble interfacial area. Recall that a lamella is a thin-liquid film that separates bubbles. Foam bubbles in porous media are as large or larger than characteristic pore size; thus, bubbles and lamellae completely span pores^{10,11}. This foam configuration is referred to as a confined foam because of the constraining effect of the porous medium on foam structure¹².

Confined gas bubbles transport by sliding over lubricating liquid films that coat pore walls¹³ and liquid-filled pore corners^{14,15}. At low bubble velocities (i.e., capillary number) characteristic of flow in porous media, the pressure drop to drive a bubble at a constant velocity exceeds that of an equivalent volume of liquid, thereby increasing the effective viscosity of the gas phase. Additionally, surfactant movement from the front of a moving bubble to the rear induces a surface-tension gradient that slows bubble motion and so increases the effective viscosity¹⁰.

The second mechanism that reduces gas mobility is trapping of the gas phase. The fraction of gas that is stationary in a foam is quantifiable using gas-phase tracers^{16,17}. Experimental measurements of trapped gas in sandstone containing foam place the fraction of gas that is not flowing between 0.85 and 0.99. The most important factors governing bubble trapping include pressure gradient, pore geometry, and foam texture; however, the dependence of trapped fraction on these factors is not established. Gillis and Radke¹⁷ find no consistent trend of trapped fraction with varying liquid or gas velocity, while Friedmann et al.¹⁶ find that the fraction of trapped gas increases slightly with gas velocity at a constant gas fractional flow.

On the pore level, gas flowing in the form of a foam tends to flow through the high permeability and high porosity zones. The wetting phase occupies the smallest pore channels. Thus, trapping of gas occurs in the intermediate-sized pores¹². Apparently, capillary forces are sufficient to immobilize a large fraction of foam bubbles¹⁸⁻²¹. Hence, pore space is blocked that would otherwise carry gas and gas relative permeability is reduced significantly.

These mobility reduction mechanisms require multiple disconnected bubbles and stable thin-liquid films between bubbles. Film stability is provided by surfactant molecules that array themselves near gas-liquid interfaces where the identically charged interfaces repel each other.

Foam films are meta-stable as opposed to

thermodynamically stable. The surfactant induced stabilizing forces are sensitive to surfactant concentration, surfactant structure, and to ionic strength of the aqueous solution. Other sources elaborate on the origin and behavior of stabilizing forces in foam films²²⁻²⁵.

Khatib et al.²⁶ first suggested that foam-film strength was directly related to gas mobility reduction in the presence of foam. For a given surfactant and concentration, they observed dramatic foam coarsening at a particular capillary pressure that they termed the "limiting capillary pressure", P_c^* . Above P_c^* , foam films are unstable, coalescence of foam lamellae is significant, and high gas mobility emerges. Below P_c^* , coalescence is significantly less and gas mobility is low. To further connect foam film stability and gas mobility, the rupture capillary pressure of single foam films was measured at a variety of surfactant and brine concentrations and compared with the steady-state pressure drops of N_2 foam in oil-free beadpacks²⁷. Stable, low mobility foam with large P_c^* was generated once the rupture pressure of individual foam films exceeded the medium capillary pressure. Detailed reviews of transport, generation, and coalescence of foam bubbles are given elsewhere^{12,22,28}.

Modeling Foam Displacement

A quantitative model is necessary to interpret the experimental results to follow. In population balance models of foam, gas mobility is computed directly from the texture or number concentration of bubbles inside porous media. Previous work has formulated a population balance approach that is mechanistic in that well documented foam mechanisms are incorporated into a continuum balance equation for foam^{29,30}. However, this approach has not been tested over a variety of surfactant concentrations and especially at low concentration where foam is weak. The population balance is chosen because of its generality and similarity to the usual continuum equations for flow of heat and mass in porous media.

In addition to the requisite material balances for water, surfactant, and nitrogen chemical species, a transient balance on the mean bubble size is written. In one dimension²⁹:

$$\frac{\partial}{\partial t} \left[\phi \left(S_f n_f + S_t n_t \right) \right] + \frac{\partial}{\partial x} \left(u_f n_f \right) = \phi S_g \left[k_1 v_w v_f^{1/3} - k_{-1} v_f n_f \right] + Q_b \quad (1)$$

where t denotes time, ϕ is porosity, S is saturation, n is bubble concentration (bubbles per unit volume of gas), u is Darcy velocity, v is the interstitial velocity ($v = u / S\phi$), k_1 is the generation rate constant, k_{-1} is the coalescence rate constant, and Q_b is a source/sink term for bubbles. The subscript f refers to flowing foam, t to trapped foam, g to the gas phase, and w to the aqueous phase. We refer to bubble concentration, foam texture, and bubble texture synonymously throughout this work.

The first term on the left of Eq. (1) is the accumulation of foam bubbles and the second term is the flux of foam bubbles.

The first term on the right of Eq. (1) represents the net generation of foam bubbles, i.e., generation minus coalescence. Foam generation is taken as a power-law expression that is proportional to the interstitial liquid velocity multiplied by the 1/3 power of the gas velocity. The origin of these velocity dependencies for generation may be found elsewhere³¹.

Foam coalesces when bubbles flow into so-called termination sites^{12,23}. Hence, foam coalescence is taken as proportional to the interstitial flux of foam, $v_f n_f$. The coalescence rate constant varies strongly with the local capillary pressure, surfactant formulation, and aqueous-phase concentration. A high rate of coalescence is expected at low surfactant concentration because there is little surfactant to exert a stabilizing effect. A dramatically lower rate is expected when the concentration is high and the surfactant is known to produce stable foam, provided that the porous medium does not exceed limiting capillary pressure.

The effects of surfactant concentration and capillary pressure are embodied in the coalescence rate constant. The following functional relationship is employed:

$$k_{-1} = k_{-1}^o \left(\frac{P_c}{P_c^* - P_c} \right)^2 \quad (2)$$

where k_{-1}^o is a scaling factor that is set constant and P_c^* is the limiting capillary pressure discussed earlier in Eq. (2). k_{-1} becomes very large as P_c and P_c^* approach equality. The major task of this work is to infer the functional form of P_c^* with respect to surfactant concentration from laboratory experiments and to simulate these experiments quantitatively.

To solve Eq. (1), additional information on the convection of foam and wetting aqueous phase is required. Darcy's law is retained including the formalism of multiphase relative permeability curves. For the gas phase, we replace viscosity with an effective viscosity relation for foam:

$$\mu_f = \mu_g + \frac{\alpha n_f}{v_f} \quad (3)$$

where α is a constant of proportionality. This expression follows directly from theoretical studies of bubble flow in capillary tubes and porous media^{14,15}.

Foam also reduces gas mobility by reducing the gas-phase relative permeability. Since the portion of gas that actually flows partitions into the largest pores with the least flow resistance, we employ a so-called "Stone-type" relative permeability model³², although the ideas employed here predate Stone³³. Hence, the relative permeability of the flowing foam is only a function of S_f . Because the wetting phase partitions selectively to the smallest pore space, the aqueous-phase relative permeability is unaffected by flowing and stationary foam. This statement is well established by experiment³⁴⁻³⁸. Aqueous phase relative permeability remains

solely a function of S_w . Clearly, the relative permeability of the stationary foam is zero. A standard exponent relative permeability model is used,

$$k_{rw} = k_{rw}^o S_{wd}^a \quad (4a)$$

$$k_{rf} = k_{rf}^o S_{fd}^b \quad (4b)$$

with a and b representing the exponents for water and gas flow, respectively. The superscript o indicates the endpoint relative permeability. The reduced saturations, S_{id} , are written

$$S_{fd} = X_f (1 - S_{wd}) \quad (5a)$$

$$S_{wd} = \frac{(S_w - S_{wir})}{(1 - S_{wir})} \quad (5b)$$

where $X_f = S_f/S_g$ is the fraction of the gas phase that is flowing and S_{wir} is the irreducible aqueous-phase saturation. The relative permeability exponents and endpoint relative permeabilities represent values for non-dispersed, continuum gas-liquid flow in the porous medium.

Experimental Setup and Procedures

The experimental program was designed to obtain an understanding of how overall recovery, pressure-drop profiles, and water saturation profiles shift with changing surfactant concentration. For this purpose, we report 5 foam flow experiments using two different packs, filled with the same sand.

The apparatus consists of a 0.51 m (20 in) long aluminum sandpack with a 0.051 m (2 in) inner diameter. It was packed with dry 100-120 mesh Ottawa sand in an upright position and pneumatic vibrators were used to ensure good settling. Screens at the inlet and outlet faces of the sandpack prevented washout of sand grains. The average porosity and permeability of pack 1 are 35% and 6.7 d, whereas for pack 2 the values are 36% and 7.0 d. CT images, as described later, confirmed that the packs were homogeneous. Permeability values reported are permeability to brine.

The sandpack attaches to an L-shaped mounting bracket for bolting of the apparatus to a precision positioning system (Compumotor, RP240, Parker Hannifin Corp.). Displacements were conducted with the core oriented horizontally.

Aluminum pressure taps were welded to the surface of the core holder. Each tap was machined to accept a Nupro 60 micron sintered filter (Swagelok, element # SS-4F-K4-60) and thereby sand migration through the tap was avoided. Pressure response was measured by a single Paroscientific pressure transducer (model 43K-101) connected to a Whitey 7-way valve (Swagelok, element # SS-43Z6). Measurement of six independent pressures is possible. The valve was switched manually and a PC was used to collect absolute pressure data from the transducer. The total acquisition time for a set of pressure data is roughly 30 to 40 s.

Nitrogen and surfactant solution are co-injected at

constant rates using a Matheson 0-10 SCCM (standard cubic centimeters per minute) mass flow meter (model 8240) and an ISCO (model 500D) syringe pump, respectively. Experiments are conducted at backpressures of roughly 690 kPa (100 psi) using a Grove Mitey-Mite dome loaded backpressure regulator (Model S-91LW).

A fourth generation (1200 fixed detectors) Picker 1200 SX X-ray computed tomography (CT) scanner is used to measure porosity and the time evolution of the in-situ water saturation. Voxel dimension (analogous to pixel size in a two-dimensional image) is 0.25 mm by 0.25 mm by 5 mm. Scans were made on 13 cylindrical volume sections perpendicular to the central axis of the core. Scan locations were not evenly spaced so that scanning through pressure ports was avoided. The acquisition time of one image is 7 s and the processing time is about 40 s. The total time of measurement is short enough to capture accurately the position of the front.

Raw CT number data is converted to porosity and saturation distribution information by subtracting the CT numbers associated with given voxels. The porosity is obtained as

$$\phi = \frac{CT_{wet} - CT_{dry}}{CT_{aq} - CT_{N_2}} \quad (6)$$

where CT denotes the CT number in Hounsfields (H). The subscript wet corresponds to a fully aqueous-phase saturated core, dry a core filled with N_2 , aq denotes the CT number for the aqueous phase, and N_2 the CT number for the gas phase. The porosity that is determined for each voxel may be displayed as an image, averaged over the cross section, or averaged over the entire core.

To construct saturation profiles we use

$$S_w = \frac{CT_{wet} - CT_{obj}}{\phi(CT_{aq} - CT_{N_2})} \quad (7)$$

where the subscript obj indicates the CT value of the object being imaged and ϕ is the independently measured porosity of each voxel. The measurement accuracy depends on the different parameters chosen for the X-ray emitter such as voltage and intensity, filters, and reproducibility of the positioning system moving the core into and out of the gantry. The measurement error of water saturation is less than 6%³⁹.

The surfactant used to make the foamer solution is an α -alpha olefin sulfonate (AOS 1416) supplied by Shell Chemical Co. Sodium chloride (NaCl) at a concentration of 0.5 wt% in distilled water was the brine. Surfactant solution concentrations employed in the experiments were 0.005, 0.01, 0.02, 0.1, and 1.0 wt active surfactant. The less concentrated solutions were prepared by diluting the 1 wt% foamer solution with a 0.5 wt% brine. The critical micelle concentration (CMC) of the solution is roughly 0.005 wt%⁹ and the nominal solution viscosity is 1 mPa s.

The experimental procedure is relatively simple. The pack was prepared and mounted on the positioning system and then N_2 was injected to assure a dry pack. The system back pressure was increased to 690 kPa (100 psi) and dry CT scans were made at the prescribed positions. Carbon dioxide (CO_2) was injected to displace the N_2 . At least 10 pore volumes of 0.005 wt% foamer solution were injected to saturate the pore space with liquid and satisfy adsorption of surfactant to the sand. The advantage of CO_2 is that it dissolves readily in water ensuring that all gas is removed. Periodically, the pressure lines were opened to purge any gas that had accumulated. Then wet CT images were collected.

The gas-liquid mixture is not foamed before injection and the injection rates are constant throughout the experiments. The foamer solution injection rate was fixed at 0.07 mL/min and the gas flow was set to 3.8 SCCM (standard cubic centimeters per minute). This translates to a superficial gas velocity of about 0.39 m/d and a gas fractional flow of 88% at the nominal system back pressure of 690 kPa. The total superficial velocity, including liquid injection, is 0.44 m/d.

Following the completion of an experiment, the core was flushed with CO_2 and then copious (10-20 PV) amounts of foamer solution of the next larger concentration were injected to resaturate the sandpack. The CT scanner was used to monitor the progress of resaturation thereby verifying that all gas had been ejected from the core. The experiments were performed in order of increasing surfactant concentration to assure that surfactant desorption from solid did not affect results. The first pack (6.7 d) was used for solutions of 0.005, 0.01, 0.02, and 1 wt% surfactant, and the second pack (7 d) was employed for the 0.1 wt % solution.

Experimental Summary

An overview is given in this section of the experimental results regarding surfactant concentration and foam displacement. The experiments demonstrate that efficiency of displacement increases with increasing surfactant solution concentration, as expected. The existence of an end effect witnessed after gas breakthrough is also pointed out. This summary motivates an in-depth evaluation and modeling study of the experiments.

Figure 1 summarizes the cumulative water recovery for each solution concentration as measured by collecting effluent from the downstream side of the back pressure regulator. Elapsed time is given nondimensionally as pore volumes (PV) which is the ratio of the total volumetric flow rate (at exit pressure) multiplied by the elapsed time and divided by the void volume of the pack. In the case of the 0.1 wt% experiment, the recovery curve was calculated by integrating the area under the water saturation profile determined by the use of CT as a function of time and adding the cumulative water injection. These saturation profiles will be described shortly. The recovery curves show an increase in the overall recovery and an increase in the time to gas breakthrough as the surfactant concentration increases. For instance, breakthrough of foam in the 0.01 wt % case occurs at about 0.60 PV and the

recovery at breakthrough is about 0.58 PV. In the case of the 1 wt% solution, the breakthrough time and the recovery at breakthrough are roughly 1.2 PV and 1.05 PV, respectively. In Fig. 1, the cumulative injected liquid is not subtracted from the cumulative production. Also, at high surfactant concentration, the pressure drops generated are large indicating gas compression. Thus, the cumulative liquid production and the breakthrough time both exceed 1 for the experiments with larger surfactant concentration.

The saturation fields across cross sections of the sandpack were computed using Eq. (7) at each scan location. Figure 2a to 2d displays typical aqueous phase saturation distributions at each of the scan locations for 1, 0.1, 0.01, and 0.005 wt% experiments, respectively. Each set of cross-sectional images was collected at about 0.5 PV of total injection. The cross section in the upper left of each set of images is nearest the inlet. Note the color bar on the right side of the figure. Color shading indicates the value of the aqueous-phase saturation. Dark blue indicates S_w equal to 0% and red indicates S_w equal to 1. White lies immediately above red on the color scale. Regions filled completely with water have a speckled red and white shading indicating the experimental error in the saturation measurement.

The blue uniform shading of Fig. 2a indicates that the foam displacement is efficient at 1 wt%. Upstream of the displacement front, the aqueous-phase saturation averages about 0.1. Also, where gas is present, it fills the entire cross section and there is no selective channeling. The images for x/L equal to 0.40 and 0.50 in Fig. 2a suggest that the saturation front is steep and sharp. The subsequent images for decreasing concentration, Figs. 2b through 2d, display similar features. However, aqueous phase saturation upstream of the front increases as the concentration decreases indicating less efficient displacement. Hence, these images corroborate the production information in Fig. 1.

The saturation change across the front becomes less sharp as the concentration decreases. For example, compare cross sections at x/L equal to 0.40 and 0.50 in Fig. 2a, 1 wt%, with the cross sections at x/L equal to 0.55 and 0.65 in Fig. 2c, 0.01 wt%. At the lower concentration, the front is more dispersed. Note that the image at x/L equal to 0.65 in Fig. 2c displays two distinct regions in the lower half of the cross section where gas has just invaded the pore space. The remaining area of the cross section is filled with aqueous solution. Figure 2d, for the 0.005 wt% concentration, displays the least uniform sweep pattern. In the fifth and sixth images ($x/L = 0.35$ and 0.40) of Fig. 2d, it is apparent that a portion of the aqueous phase solution is not displaced from the top of the sandpack.

All of the experiments proceeded as expected prior to breakthrough. After breakthrough, evidence of end effects was witnessed in both the saturation distributions and in pressure profiles. Figure 3 presents the steady-state, one-dimensional, aqueous-phase saturation profiles as a function of distance along the pack. The saturation values were obtained by determining the water saturation in each voxel of a cross section and then averaging. Different symbols indicate

experiments at different surfactant concentration and the dashed lines merely connect the individual points. For the 1 and 0.1 wt% experiments, the steady aqueous phase saturation is below 0.15 and relatively uniform throughout the sand pack. At the lower concentrations (0.02, 0.01, and 0.005 wt%), the aqueous phase saturation is clearly larger near the outlet than it is in the center of the column. The effect becomes more pronounced as surfactant solution concentration decreases. This signifies a classic capillary end effect where the porous medium retains water in an attempt to maintain equilibrium across the outlet where the capillary pressure is zero or near zero⁴⁰⁻⁴².

A second type of end effect, or a different manifestation of a capillary end effect, was witnessed in the high surfactant concentration experiments, as illustrated in Fig. 4 for 1 wt% solution. Here the pressure-drop profile along the length of the core is plotted as a function of time. Different symbols are associated with different times and dashed lines connect pressure data points to guide the eyes. As indicated by the figure, the gas breakthrough time is between 1.2 and 1.4 PV. Pressure gradients prior to breakthrough are always steepest in the foam-filled region and shallowest in the aqueous-phase filled region. After breakthrough, the steepest pressure gradients are found near the outlet. Comparing times of 1.4, 2.9, and 6.5 PV, it is found that the region of the pack where the pressure gradient is steepest expands from the outlet toward the inlet. At 1.4 PV, the pressure gradient is steepest between x/L equal to 0.7 and 1, whereas at 1.9 PV, the steep gradient extends from x/L equal to 0.45 to 1. At 6.5 PV, the pressure drop over the pack is about 580 kPa (84 psi). The experiments at 0.1 wt% concentration display a similar behavior post breakthrough, although not shown here.

An additional feature is the length of time to achieve a steady-state pressure profile. Previous experiments in sandstone with AOS at about 1 wt% concentration employing similar injection rates, and no end effect, reached steady state in about 2 PV²⁹. The long time to reach steady state in the current experiments results because the pressure drop across the core builds from the outlet toward the inlet. Since this occurs against the direction of flow, it is a slow process.

Transient Displacements

To model the transient foam displacements, Eqs. (1) through (5) are solved with a standard fully-implicit, simultaneous-solution finite difference method using upstream weighting of the phase mobilities⁴³. Additionally, water and nitrogen balances are computed. Since the sand packs are presaturated with surfactant solution, there is no need to compute a surfactant mass balance. The unknown primitive variables are pressure, gas-phase saturation, and bubble density. Boundary and initial conditions mirror the experiments: gas and liquid are injected at constant mass rates and the outlet pressure is fixed at 690 kPa (100 psi). The surfactant and gas are not foamed before injection. Therefore, no bubbles are injected and Q_b is set to zero. The initial conditions include S_w equal to 1, n_f equal to 0, and the appropriate uniform surfactant

concentration depending upon the experiment under consideration.

Tables 1 and 2 list the model parameters including standard multiphase flow information as well as population balance parameters. Also given in Table 1 is the capillary pressure versus water saturation function. The ratio of foam generation to coalescence rate constants, $k_1/k_{c,1}$, was chosen to yield bubbles with undistorted spherical radii of about 0.4 mm for the 1 wt% case. Further information on parameter estimation for population balance models is discussed in some detail elsewhere^{12,29}.

The critical capillary pressure, P_c^* , as a function of surfactant concentration is required to simulate the experiments. Since the surfactant concentration in each experiment is constant, we find P_c^* for each concentration rather than assuming a functional form for P_c^* versus surfactant concentration. Table 2 lists the value of P_c^* for each concentration and the surface tension as a function of concentration for this particular surfactant at a brine concentration of 0.5 wt%. As expected, P_c^* is large when the surfactant concentration is large and decreases as the concentration approaches the CMC²⁷.

The modeling results for foam texture evolution at each surfactant concentration are presented first. Unfortunately, no experimental method exists to measure directly foam texture in situ. Strong foam at high surfactant concentration is shown first and then subsequent simulations at lower concentration follow. Next, the effect of foam texture on gas mobility is judged from measured and computed aqueous-phase saturation profiles as a function of time. Pressure drop profiles and the match between experiment and model complete this section.

Foam Texture

The predicted bubble concentration along the length of the core as a function of time is given for each of the different surfactant concentrations in Fig. 5. Figure 5a represents the largest concentration while Fig. 5e shows the lowest. Time is given nondimensionally in pore volumes of total injection with the exit pressure used to calculate the volumetric gas rate. In Fig 5a, representing the 1 wt% concentration experiment, a region of net generation is found near the inlet. Bubble concentration is nearly constant at all time levels beyond roughly the first quarter of the sand pack until the concentration peaks immediately upstream of the front. Physically, the net rate of foam generation is large at the front. Thus, the bubble concentration goes through a maximum before decreasing to zero downstream of the front where there is no gas, and hence, no bubbles³⁰. The relatively constant foam concentration between the inlet region and the foam front is about 22 bubbles/mm³. A foam bubble of this size has a diameter of roughly 0.44 mm when taken out of the porous medium and allowed to assume a spherical shape. For the simulation of the 1 wt% concentration, the breakthrough time of bubbles is about 1.2 PV. This agrees well with the cumulative liquid production information in Fig. 1.

The bubble concentration profiles shown in Fig. 5b for the

0.1 wt% concentration are lower than the values for the 1 wt% case. The lower surfactant concentration results in a lesser critical capillary pressure for foam coalescence, as given in Table 2. As a result, the foam coalescence rate increases and the average bubble concentration decreases. Disregarding the inlet region and the elevation of bubble concentration at the front, the flowing bubble concentration in this case is about 3.5 bubbles/mm³ corresponding to an undistorted spherical bubble diameter of 0.82 mm.

For the lowest concentrations in Figs. 5c through 5e, the bubble concentration gradually approaches zero with declining surfactant concentration. In Fig. 5c for the 0.02 wt% case, the texture upstream of the spike in bubble concentration at the front is only 0.4 bubbles/mm³ while in Figs. 5d and 5e for the 0.01 and 0.005 wt% solutions, the bubble concentration in this region is only negligibly greater than zero (20×10^{-8} mm⁻³). The spherical bubble diameters corresponding to these textures are 1.7 mm for the 0.02 wt% case and essentially infinite for the smallest concentrations. In the limit of no foam, continuous gas results and infinitely large bubbles emerge.

An elevation in foam texture in the region of the front is also found in the lower surfactant concentration cases. The process of snap-off of gas bubbles is purely mechanical and continues regardless of the concentration of surfactant. This is reflected in the net foam generation rate of Eq. (1). As a consequence, bubbles are always generated when the water saturation is high and the capillary pressure is less than critical such as when gas first enters a water saturated region of the porous medium. Foam coalescence forces quickly destroy most of this initial foam because the surfactant concentration is low and thus the limiting capillary pressure for foam coalescence is reached quickly. Correspondingly, the magnitude of the elevation in foam texture at the front also decreases with decreasing surfactant concentration. In Fig. 5c the maximum texture is 8 bubbles/mm³ while in Fig. 5d it is 4 bubbles/mm³. There is little difference in the bubble texture profiles of Figs. 5d and 5e because the limiting capillary pressure, as given in Table 2, has changed little between these two cases.

Aqueous Phase Saturation

The one-dimensional aqueous-phase saturation profiles as a function of time for each case are presented in Fig. 6. Time is again given nondimensionally in pore volumes. One dimensional saturation data is obtained by averaging the voxel by voxel CT-measured saturations for each cross section. In Fig. 6, symbols give the experimentally measured points and they are connected by dashed lines to guide the eye. The solid lines represent model predictions based upon the foam textures in Fig. 5 and Eqs. (3) to (5) for gas mobility. In general, transient displacement is efficient where bubble concentrations are large such as in the 1 wt% surfactant concentration case in Fig. 6a, and displacement efficiency decreases as surfactant concentration and bubble texture decrease. Also note that the saturation change across the front is steep and sharp when the foam is strong, as shown in Figs 6a and 6b.

The match between experiment and model is quite good in all cases, except perhaps the 0.005 wt% case, prior to breakthrough and the development of end effects. Displacement efficiency correctly declines with decreasing concentration of surfactant solution in the simulations. Also, notice that the predicted saturation profiles across the displacement front in Figs. 6c through 6e become more diffuse as the surfactant concentration decreases. Predictions echo experiment in this regard. It is important to recall that these results are not achieved by history matching each experiment. The only parameter that changes in each simulation is the value of P_c^* . This parameter is physical and directly related to surfactant concentration²⁷.

Regarding the 0.005 wt% experiment summarized in Fig. 6e, a region exists at x/L roughly equal to 0.35 where desaturation of the aqueous phase is slow. The aqueous phase saturation distribution at this cross section of the sandpack is illustrated in the image at x/L equal to 0.35 in Fig. 2d. Displacement is not uniform across the cross section, and a region of 100 % aqueous phase saturation remains. Hence, the experiment and simulation results do not agree. Nevertheless, the simulations reproduce, qualitatively, the low displacement efficiency at this surfactant concentration.

Capillary end effects are evident in the evolution of the experimental water saturation profile in Figs. 6d and 6e. In Fig. 6d, breakthrough of gas at the outlet occurs between 0.4 and 0.6 PV. Following breakthrough there is little desaturation of the final third of the core; the saturation data at 0.6 and 1 PV in this region nearly overlay each other. Similar behavior is found for the 0.005 wt% experiment. The foam simulations do not incorporate end effects and so cannot match the post breakthrough saturation distributions.

Pressure Drop

The second type of in-situ data collected was pressure drop. The lower limit of accuracy for the pressure measurement system used is about 0.14 to 0.34 kPa (0.02 to 0.05 psi). Experimental and simulated pressure drop profiles as a function of time are presented in Fig. 7 for each of the surfactant concentrations. The match between model and experiment is acceptable. Large bubble concentrations lead to significant gas-phase flow resistance and low aqueous-phase saturation. Therefore, the 1 wt% case with the finest bubble texture, as shown in Fig. 5a, demonstrates the largest overall pressure drop. As the bubble textures decline with surfactant concentration, the predicted pressure drops decline also.

For the 1 wt% and 0.1 wt% cases in Figs. 7a and 7b where significant foam and pressure drops are generated, it is easy to distinguish the foam-filled region of the sand pack in the pressure drop profiles. For example in Fig. 7b at 0.41 PV, a relatively steep pressure gradient due to the presence of foam extends from the inlet to x/L equal to 0.43. The pressure drop in the remainder of the sand pack is small corresponding to the single-phase flow of water.

To improve the clarity of Figs. 7c to 7e, the time corresponding to each simulated pressure profile is marked on

the curve and a legend displays the symbol and time corresponding to each experimental data point. Difficulties were encountered in measuring pressure drops at the lower surfactant concentrations, especially at the inlet of the sandpack. Likely, some gas migrated into the pressure line during the experiment. This makes accurate pressure measurement difficult. Accordingly, erroneous pressure information has been deleted from Figs. 7d and 7e. In these instances, large, aphysical, positive pressure gradients were measured. The portion of the data presented in Fig. 7c that is in error is not clear, so all information is retained. Despite these problems, experiment and simulation agree on the general magnitude of pressure drop.

A feature of the model that bears further discussion is the predicted pressure drop profiles for the low surfactant concentration cases in the region immediately upstream of the foam front. Examine the pressure profile at 0.44 PV in Fig. 7c and the corresponding bubble concentration profile in Fig. 5c. The pressure gradient is relatively shallow in the foam-filled region except immediately before the front. Here, the gradient is much steeper than in the front region because bubble concentration is elevated at the front. This elevation in texture reduces gas mobility causing the pressure gradient to steepen.

End Effect

The end effect evident in the saturation profiles of Fig. 3 for low surfactant concentrations (0.005, 0.01, and 0.02 wt%) is similar in origin to the capillary end effects described elsewhere for regular two-phase flow⁴⁰⁻⁴². Hence, we do not attempt to analyze this effect here. The origin is far less clear of the end effect whereby the pressure gradient steepens from the outlet against the direction of flow toward the inlet, as illustrated in Fig. 4 for the 1 wt% concentration case. The steady aqueous-phase saturation profiles given in Fig. 3 for the 0.1 and 1 wt% cases demonstrate very low S_w near the sand pack outlet and so do not appear to be classic capillary end effects. Of course, there are no measurements at x/L equal to 1 and S_w might increase immediately before the outlet.

We will use the population balance approach and some simplifying assumptions drawn from the experimental results to probe the origin of the end effect witnessed at 0.1 and 1 wt% surfactant concentrations. First, the Darcy velocity of the compressible foamed gas phase is written as

$$u_f = \frac{p_{sc} u_{f,sc}}{p_g} = \frac{-kk_{rf}}{\mu_f} \frac{dp_g}{dx} \quad (8)$$

where the subscript sc refers to reference or standard conditions. For large foam bubble concentration such as the 1 and 0.1 wt% concentration experiments, the gas viscosity contribution in Eq. (3) for effective foam viscosity is negligible and

$$\mu_f = \frac{\alpha n_f}{u_f^{1/3}} (\phi X_f S_g)^{1/3} \quad (9)$$

In Eq. (9), the interstitial velocity has been replaced by $u_f/\phi X_f S_g$. Some knowledge of the foam texture is necessary to employ Eq. (9) in Eq. (8). Recall, that roughly 6 PV are required for the pressure to reach a steady state. Thus, the conditions within the core evolve quite slowly after gas breakthrough and local equilibrium holds approximately. Setting the expression for the net generation of foam in Eq. (1) to zero, replacing interstitial velocity with Darcy velocity and the appropriate phase saturations, and solving for foam texture one obtains

$$n_f = \left(\frac{k_1}{k_{-1}} \right) \left(\frac{u_w}{\phi S_w} \right) \left(\frac{\phi X_f S_g}{u_f} \right)^{2/3} \quad (10)$$

Substituting Eqs. (9) and (10) into Eq. (8), recognizing that $p_{sc} u_{f,sc}$ equals $p_g u_f$, and integrating with respect to pressure yields

$$\frac{k_{rf}}{X_f S_g} = \Delta x \left(\frac{\alpha k_1}{k k_{-1}} \right) \left(\frac{u_w}{S_w} \right) \frac{1}{\Delta p_g} \quad (11)$$

where Δp_g is the pressure drop and Δx the distance between discrete points. Of the quantities in Eq. (11), Δp_g , S_g , S_w , u_w , k , and Δx are directly measurable; α and k_1 are assumed to be equal to their values in Table 1; and k_{rf} and k_{-1} are functions of the unknown X_f and measured S_g . Thus, the only unknown quantity in Eq. (11) is the flowing foam fraction, X_f .

Figure 8 displays the result of applying Eq. (11) to the pressure information in Fig. 4 and the CT-scan determined phase saturations. The step changes in X_f evident in the profiles of Fig. 8 are a result of the pressure drop measurements over different regions of the sandpack. On average, the flowing fraction is about 0.04 at steady state, 5.2 PV. Near the outlet the flowing foam fraction is low at all times. Progressively, the flowing foam fraction decreases between 1.3 and 5.3 PV of injection. As indicated by Eqs. (4b) and (5), foam relative permeability decreases as X_f decreases and the pressure drop correspondingly increases. Reductions in X_f occur first near the outlet and at later times near the inlet. Thus, pressure gradients increase first in the vicinity of the outlet.

Information from between the first two pressure taps has been excluded. Near the inlet, net foam generation occurs, as shown in Fig. 5, and the application of local equilibrium is not correct.

Figure 9 displays the results of applying this analysis to the results of the 0.1 wt% concentration experiment. Again, X_f decreases slowly over time and reductions occur first at the outlet and progress toward the inlet.

Conclusion

An experimental study of foam generation and propagation as a function of aqueous surfactant concentration was conducted in $7 \mu\text{m}^2$, homogeneous sand packs. The in-situ phase

saturation and pressure distribution were measured during the experiments. As expected, it is found that displacement efficiency decreases and gas mobility increases with decreasing surfactant concentration. This experimental trend indicates that foam weakens as the surfactant concentration decreases. However, even weak foam improves displacement somewhat.

Such results are best understood considering the role of foam bubble size, or synonymously foam texture, in setting the mobility of foamed gas in porous media. Many small bubbles result in a low mobility foam and few large bubbles result in a high mobility foam. Foam bubbles, at fixed injection rates of liquid and gas, grow in volume as surfactant concentration decreases because foam coalescence forces are inversely proportional to surfactant concentration.

These ideas are expressed quantitatively by the incorporation of the role of foam texture on displacement in porous media using a mechanistic, mean, bubble-size conservation equation. In essence, foam is treated as a nonchemical, reactive, component of the gas phase and the evolution of foam texture is modeled explicitly using rate equations for foam generation and coalescence. Coalescence as a function of surfactant concentration is modeled employing the notion of limiting capillary pressure for foam stability. That is, the maximum suction capillary pressure that foam films can withstand decreases with surfactant concentration. The foam bubble population balance model predicts accurately the location of saturation and pressure fronts across the range of concentrations studied. This is achieved by properly accounting for limiting capillary pressure as a function of aqueous surfactant concentration and without parameter adjustment.

The post breakthrough behavior exhibited in the experiments indicates the presence of an end effect. The end effect is similar to a classic capillary end effect for low surfactant concentration. At larger concentrations, the end effect results in the pressure gradient building from the outlet, against the direction of flow, toward the inlet. Many pore volumes of fluid injection are necessary to achieve steady state even at moderate to high surfactant concentrations and these long times are attributed to such end effects.

Nomenclature

CT	CT number
k	rate constant
k_r	relative permeability
n	number density of foam
p	pressure
P_c	capillary pressure
Q_b	source/sink term for bubbles
S	phase saturation
t	time
u	Darcy phase velocity
v	interstitial phase velocity
x	distance
X	foam fraction

subscripts

$l, -l$	generation, coalescence rate constant
a, b	exponents for phase relative permeability
aq	CT number for the aqueous phase
d	normalized phase saturation
<i>dry</i>	CT number for dry porous medium
f	flowing foam
g	gaseous phase
N_2	CT number for nitrogen
<i>obj</i>	CT number, general
ir	irreducible phase saturation
t	time
w	aqueous phase
<i>wet</i>	CT number for wet porous medium

superscripts

o	reference value
*	limiting capillary pressure

Greek

α	proportionality constant
ϕ	porosity
σ	surface tension
μ	viscosity

Acknowledgement

This work was supported by the Assistant Secretary for Fossil Energy, Office of Oil Gas and Shale Technologies of the U.S. Department of Energy under Contract No. DE-FG22-96BC14994 to Stanford University. Likewise the support of the SUPRI-A Industrial Affiliates is acknowledged.

Acknowledgement is made to the donors of The Petroleum Research Fund, administered by the ACS, for partial support of this research.

References

1. Wunderlich, R.W., J.C. Fountain, and R.E. Jackson: "In Situ Remediation of Aquifers Contaminated with Dense Nonaqueous Phase Liquids by Chemical Enhanced Solubilization," *J. Soil Contamination* (**1** 1992), 361-378.
2. Hirasaki, G.J., C.A. Miller, R. Szafranski, J.B. Lawson, and N. Akiya: "Surfactant/Foam Process for Aquifer Remediation," paper SPE 37257, presented at the SPE International Symposium on Oilfield Chemistry, Houston, TX Feb 18-21, 1997.
3. Hirasaki, G.J., C.A. Miller, R. Szafranski, J.B. Lawson, D. Tanzil, R.E. Jackson, J. Londergan, and H. Meinardus: "Field Demonstration of the Surfactant/Foam Process for Aquifer Remediation," paper SPE 39393, presented at the SPE Ann. Tech. Conf. and Exhibition, San Antonio, TX Oct 5-8, 1997.
4. Patzek, T.W.: "Field Application of Steam Foam for Mobility Improvement and Profile Control," *Soc. Pet. Eng. Res. Eng.* (**11** 1996), 79-85.
5. Hoefner, M.L., E.M. Evans, J.J. Buckles, and T.A. Jones: "CO₂ Foam: Results from Four Developmental Field Trials," paper SPE/DOE 27787, presented at the SPE/DOE Ninth Symposium on Improved Oil Recovery, Tulsa, Oklahoma April 17-20, 1994.
6. Aarra, M.G., A. Skauge, S. Sognesand, and M. Stenhaug: "A Foam Pilot Test Aimed at Reducing Gas Inflow in a Production Well at the Oseberg Field," *Petroleum Geoscience* (**2** 1996), 125-132.
7. Bergeron, V., M.E. Fagan, and C.J. Radke: "Generalized Entering Coefficients - A Criterion for Foam Stability Against Oil in Porous Media," *Langmuir* (**9** 1993), 1704-1713.
8. Myers, T.J. and C.J. Radke: "Transient Foam Displacement in the Presence of Residual Oil: Experiment and Simulation Using a Population-Balance Model.," paper SPE 56412, presented at the SPE Ann. Tech. Conf. and Exhibition, Houston, TX 3-6 October, 1999.
9. Bertin, H.J., O.G. Apaydin, L.M. Castanier, and A.R. Kovalchuk: "Foam Flow in Heterogeneous Porous Media: Effect of Crossflow," *Soc. Pet. Eng. J.* (**4** 1999), to appear.
10. Hirasaki, G.J. and J.B. Lawson: "Mechanisms of Foam Flow in Porous Media: Apparent Viscosity in Smooth Capillaries," *SPEJ* (**25** 1985), 176-190.
11. Ettinger, R.A. and C.J. Radke: "Influence of Foam Texture on Steady Foam Flow in Berea Sandstone," *Soc. Pet. Eng. Res. Eng.* (**7** 1992), 83-90.
12. Kovalchuk, A.R. and C.J. Radke: "Fundamentals of Foam Transport in Porous Media", *Foams in the Petroleum Industry*, L.L. Schramm, Editor. , American Chemical Society, Washington, D.C. (1994) p. 115-163.
13. Bretherton, F.P.: "The Motion of Long Bubbles in Tubes," *J. Fluid Mech.* (**10** 1961), 166-188.
14. Wong, H., C.J. Radke, and S. Morris: "The Motion of Long Bubbles in Polygonal Capillaries: I. Thin Films," *J. Fluid Mech.* (**292** 1995), 71-95.
15. Wong, H., C.J. Radke, and S. Morris: "The Motion of Long Bubbles in Polygonal Capillaries: II. Drag, Fluid Pressure, and Fluid Flow," *J. Fluid Mech.* (**292** 1995), 95-110.
16. Friedmann, F., W.H. Chen, and P.A. Gauglitz: "Experimental and Simulation Study of High-Temperature Foam Displacement in Porous Media," *Soc. Pet. Eng. Res. Eng.* (**6** 1991), 37-45.
17. Gillis, J.V. and C.J. Radke: "A Dual-Gas Tracer Technique for Determining Trapped Gas Saturation During Steady Foam Flow in Porous Media," paper SPE 20519, presented at the 65th SPE Annual Technical Conference, New Orleans, LA September, 1990.
18. Cohen, D., T.W. Patzek, and C.J. Radke: "Onset Of Mobilization and The Fraction Of Trapped Foam In Porous Media," *Transport in Porous Media* (**28** 1997), 253-284.
19. Kharabaf, H. and Y.C. Yortsos: "Pore Network Model for Foam Formation and Propagation in Porous Media," *Soc.*

- Pet. Eng. J.* (3 1998), 42-53.
20. Hanssen, J.E.: "Foam as a Gas-Blocking Agent in Petroleum Reservoirs. II: Mechanisms of Gas Blockage," *Journal of Petroleum Science & Engineering* (10 1993), 135-156.
 21. Rossen, W.R. and P.A. Gauglitz: "Percolation Theory and Mobilization of Foams in Porous Media," *Am. Inst. Chem. Eng. J.* (37 1990), 1176-1188.
 22. Chambers, K.T. and C.J. Radke: "Capillary Phenomena in Foam Flow Through Porous Media", *Interfacial Phenomena in Petroleum Recovery*, N.R. Morrow, Editor. , Marcel Dekker Inc., New York (1991) p. 191-255.
 23. Jiménez, A.I. and C.J. Radke: "Dynamic Stability of Foam Lamellae Flowing Through a Periodically Constricted Pore", *Oil-Field Chemistry: Enhanced Recovery and Production Stimulation*, J.K. Borchardt and T.F. Yen, Editors. , American Chemical Society, Washington, D.C. (1989) p. 460-479.
 24. Hirasaki, G.J.: "Thermodynamics of Thin Films and The Three-Phase Contact Regions", *Interfacial Phenomena in Petroleum Recovery*, N.R. Morrow, Editor. , Marcel Dekker Inc., New York (1991) p. 23-76.
 25. Vrij, A.: "Possible Mechanism for the Spontaneous Rupture of Thin, Free Liquid Films," *Disc. Faraday Soc.* (42 1966), 22-33.
 26. Khatib, Z.I., G.J. Hirasaki, and A.H. Falls: "Effects of Capillary Pressure on Coalescence and Phase Mobilities in Foams Flowing Through Porous Media," *Soc. Pet. Eng. Res. Eng.* (3 1988), 919-926.
 27. Aronson, A.S., V. Bergeron, M.E. Fagan, and C.J. Radke: "The Influence of Disjoining Pressure on Foam Stability and Flow in Porous Media," *Colloids and Surfaces A: Physicochemical Eng. Aspects* (83 1994), 109-120.
 28. Rossen, W.R.: "Foams in Enhanced Oil Recovery", *Foams: Theory, Measurements and Applications*, R.K. Prud'homme and S. Khan, Editors. , Marcel Dekker, New York (1995).
 29. Kovscek, A.R., T.W. Patzek, and C.J. Radke: "A Mechanistic Population Balance Model For Transient and Steady-State Foam Flow in Boise Sandstone," *Chem. Eng. Science* (50 1995), 3783-3799.
 30. Kovscek, A.R., T.W. Patzek, and C.J. Radke: "Mechanistic Foam Flow Simulation in Heterogeneous Multidimensional Porous Media," *SPEJ* (2 1997), 511-526.
 31. Kovscek, A.R. and C.J. Radke: "Gas Bubble Snap-Off Under Pressure-Driven Flow in Constricted Noncircular Capillaries," *Colloids and Surfaces A: Physicochemical and Engineering Aspects* (117 1996), 55-76.
 32. Stone, H.L.: "Probability Model for Estimating Three-Phase Relative Permeability," *J. Pet. Tech.* (22 1970), 214-218.
 33. Saraf, D.N. and I. Fatt: "Three-Phase Relative Permeability Measurement Using a Nuclear Magnetic Resonance Technique for Estimating Fluid Saturation," *Soc. of Pet. Eng. J.* (9 1967), 235-242.
 34. Bernard, G.G., L.W. Holm, and L.W. Jacobs: "Effect of Foam on Trapped Gas Saturation and on Permeability of Porous Media to Gas," *Soc. Pet. Eng. J.* (5 1965), 295-300.
 35. Holm, L.W.: "The Mechanism of Gas and Liquid Flow Through Porous Media in the Presence of Foam," *Soc. Pet. Eng. J.* (8 1968), 359-369.
 36. Huh, D.G. and L.L. Handy: "Comparison of Steady- and Unsteady-State Flow of Gas and Foaming Solution in Porous Media," *Soc. Pet. Eng. Res. Eng.* (4 1989), 77-84.
 37. De Vries, A.S. and K. Wit: "Rheology of Gas/Water Foam in the Quality Range Relevant to Steam Foam," *Soc. Pet. Eng. Res. Eng.* (5 1990), 185-192.
 38. Sanchez, J.M., R.S. Schechter, and A. Monsalve: "The Effect of Trace Quantities of Surfactant on Nitrogen/Water Relative Permeabilities," paper SPE 15446, presented at the 61st SPE Annual Technical Conference, New Orleans, LA October, 1986.
 39. Akin, S., M.R.B. Demiral, and E. Okandan: "A Novel Method of Porosity Measurement Utilizing Computerized Tomography," *In Situ* (20 1996), 347-365.
 40. Kyte, J.R. and L.A. Rapoport: "Linear Waterflood Behavior and End Effects in Water-Wet Porous Media," *Petroleum Transactions, AIME* (213 1958), 423-426.
 41. Perkins, F.M.J.: "An Investigation of the Role of Capillary Forces in Laboratory Waterfloods," *Petroleum Transactions, AIME* (210 1957), 409-411.
 42. Douglas, J.J. and R.J. Wagner: "Calculation of Linear Waterflood Behavior Including the Effects of Capillary Pressure," *Petroleum Transactions, AIME* (213 1958), 96-102.
 43. Aziz, K. and A. Settari: *Petroleum Reservoir Simulation*. , Applied Science Publishers LTD, London, (1979) 125-199.

Table 1. Parameter values.

Two-phase flow parameters		Population balance parameters	
parameter	value	parameter	value
k	7 μm ²	k ₁	7.5 x 10 ¹² s ^{1/2} m ^{-13/3}
φ	0.35	k ^o ₋₁	100 m ⁻¹
a	3	α	2.5 x 10 ⁻¹⁴ Pas ^{2/3} m ^{10/3}
b	1.8	X _f	0.10
k ^o _{rw}	0.7		
k ^o _{rg}	1	Capillary pressure function	
S _{wir}	0.06	$P_c = \sigma \sqrt{\frac{\phi}{k}} (1.417(1 - S_{wd}) - 2.120(1 - S_{wd})^2 + 1.263(1 - S_{wd})^3)$	
μ _w	1.0 mPa-s		
μ _g	0.018 mPa-s		

Table 2. Limiting capillary pressure and surface tension values (σ from Bertin et al. (1999)).

Concentration (wt%)	σ (mN/m)	P _c [*] (kPa)
1.0	31.1	30.4
0.10	31.9	17.6
0.020	32.8	7.19
0.010	33.1	3.67
0.005	34.0	2.34

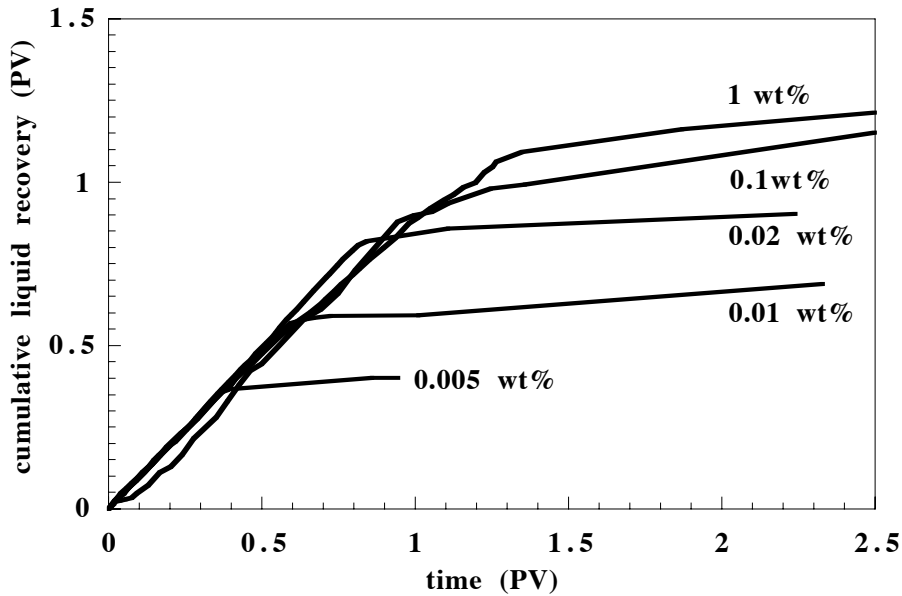


Fig. 1-- Cumulative water recovery.

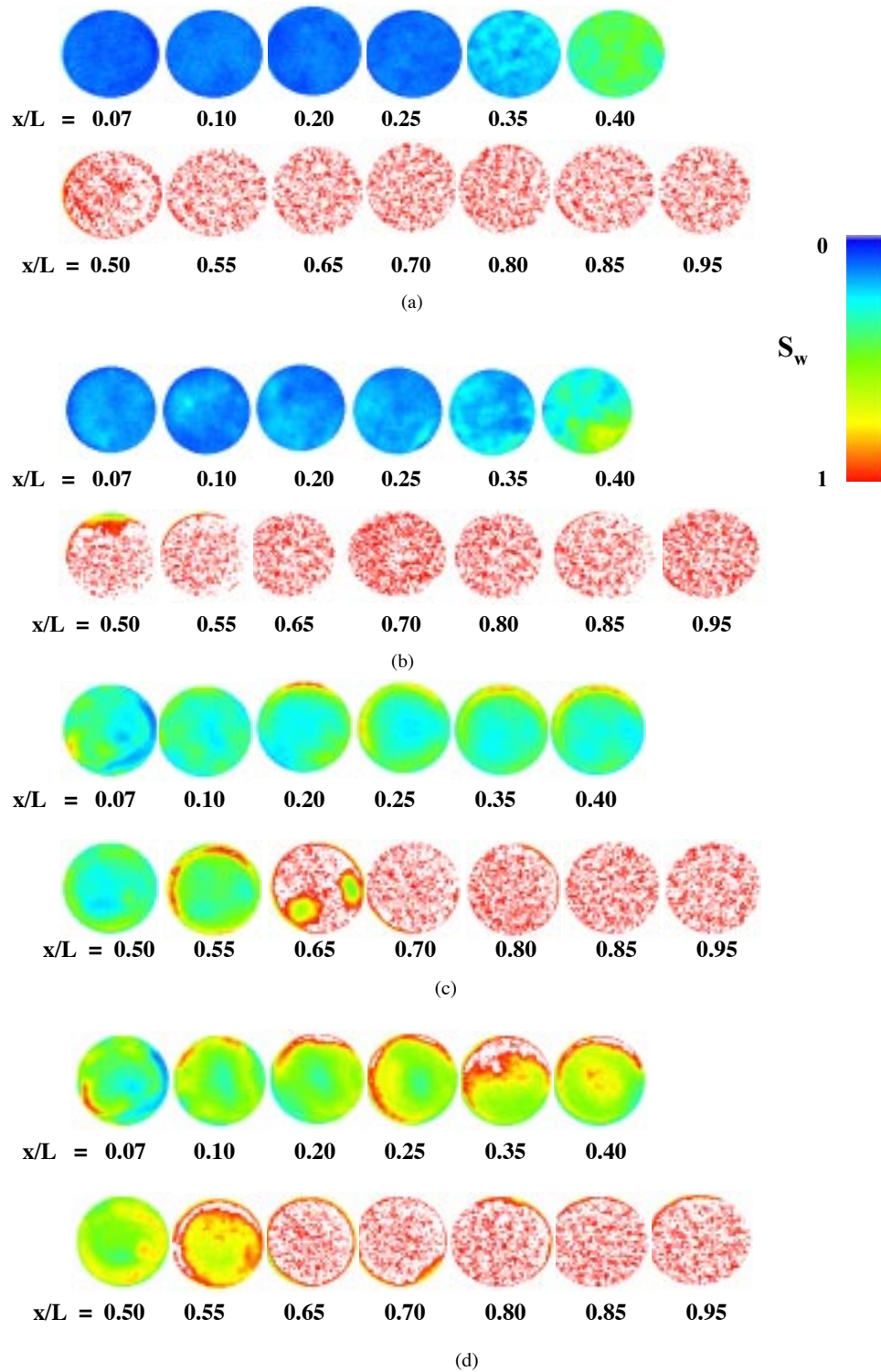


Fig. 2--Water saturation in cross sections along the length of the sandpack. Below each image the position of the cross section is given (a) 1 wt% case at 0.52 PV; (b) 0.1 wt% case at 0.51 PV; (c) 0.01 wt% case at 0.51 PV; (d) 0.005 wt% case at 0.55 PV.

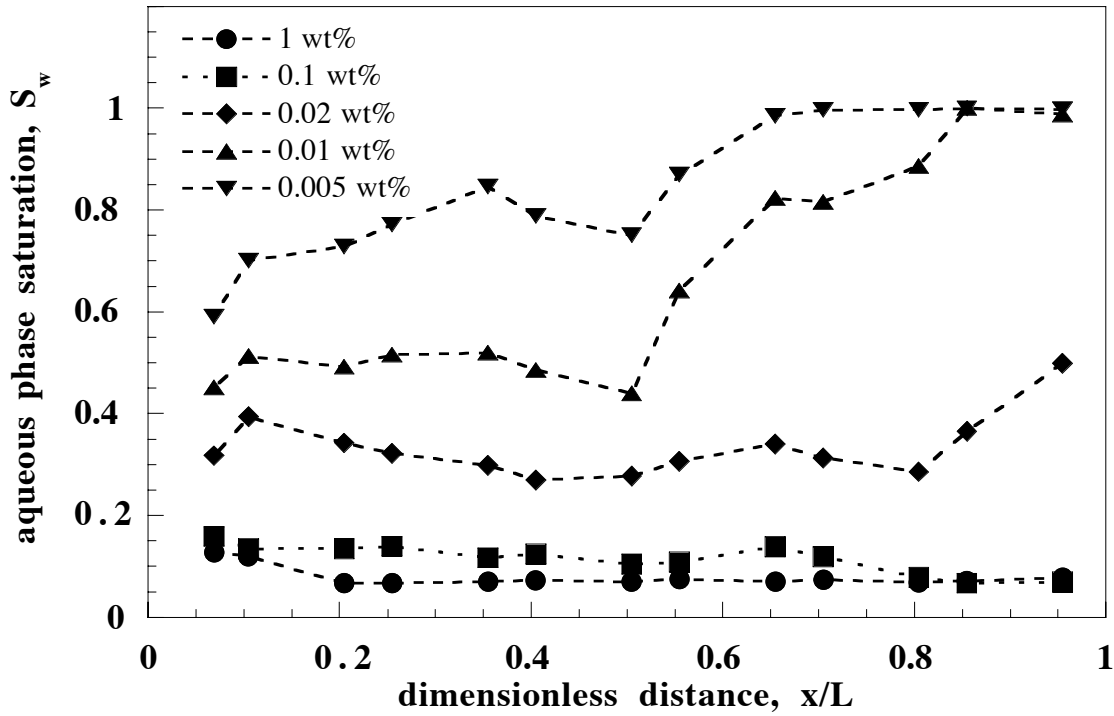


Fig. 3--Steady state aqueous-phase saturation profiles.

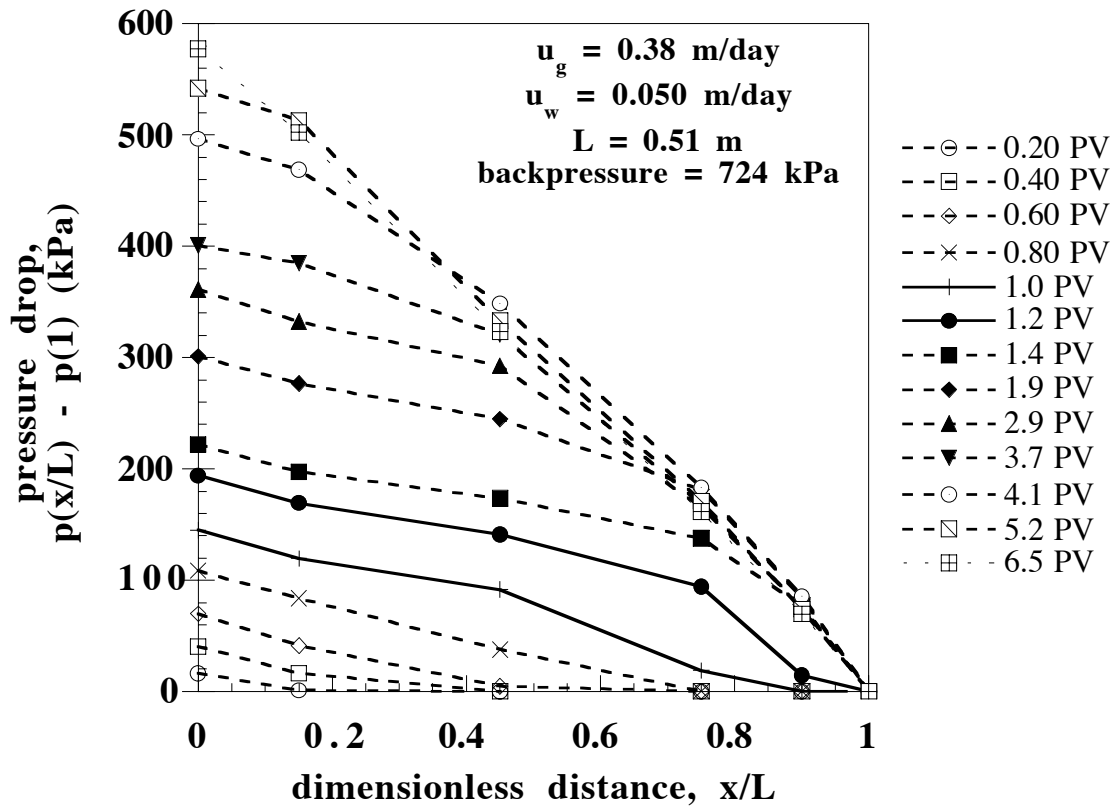


Fig. 4--Experimental transient pressure profiles, 1 wt% case.

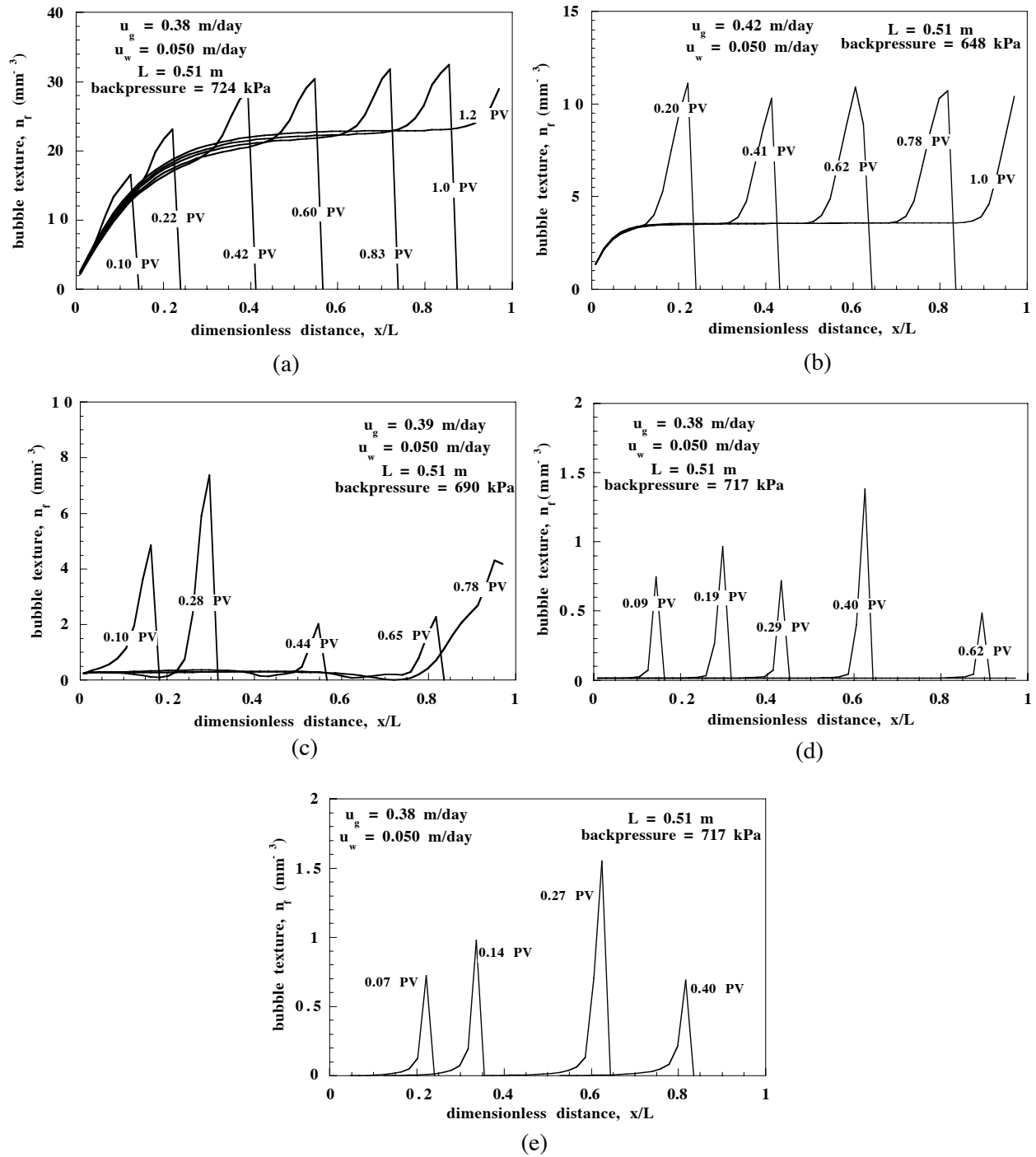


Fig. 5--Model transient flowing bubble texture profiles (a) 1 wt% case; (b) 0.1 wt% case; (c) 0.02 wt% case; (d) 0.01 wt% case; (e) 0.005 wt% case.

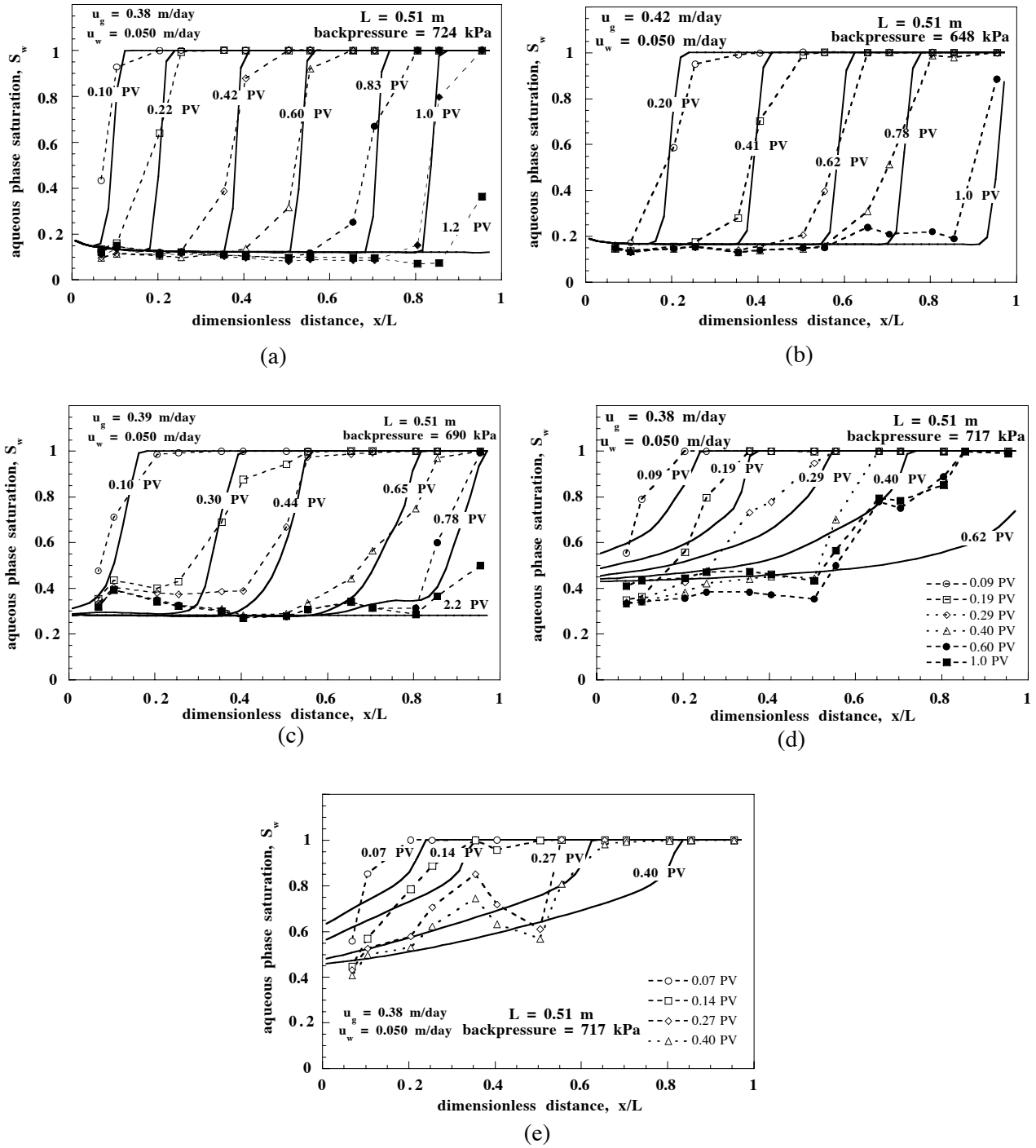


Fig. 6--Experimental (symbols connected by dashed lines) and model (solid lines) transient aqueous-phase saturation profiles. (a) 1 wt% case; (b) 0.1 wt% case; (c) 0.02 wt% case; (d) 0.01 wt% case; (e) 0.005 wt% case.

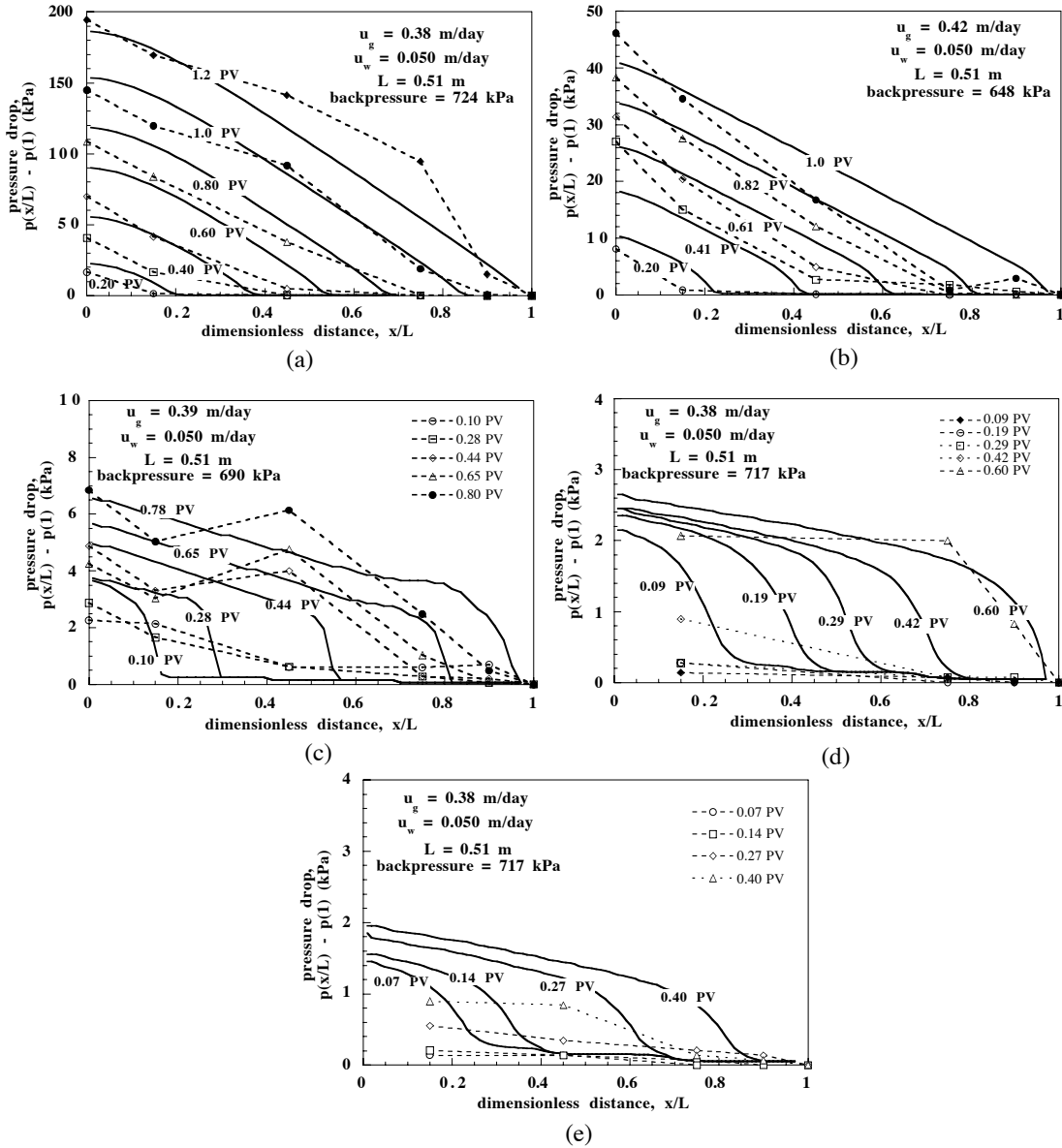


Fig. 7--Experimental (symbols connected by dashed lines) and model (solid lines) transient pressure profiles. (a) 1 wt% case; (b) 0.1 wt% case; (c) 0.02 wt% case; (d) 0.01 wt% case; (e) 0.005 wt% case.

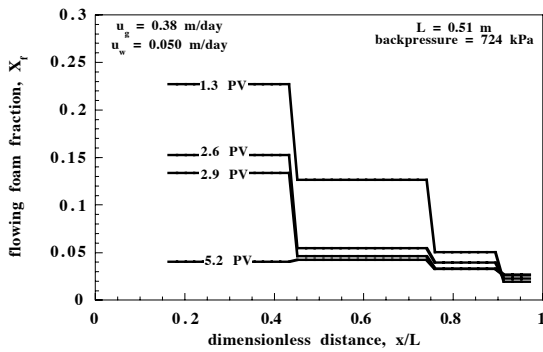


Fig. 8--Flowing foam fraction profiles based upon a local equilibrium assumption, 1 wt% case.

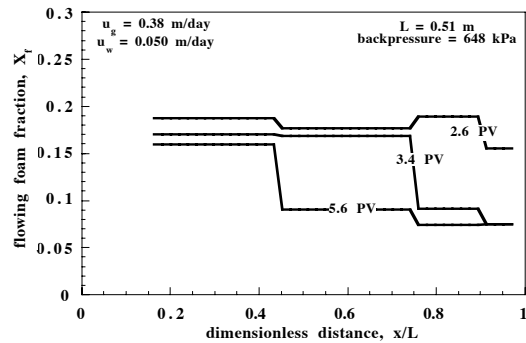


Fig. 9--Flowing foam fraction profiles based upon a local equilibrium assumption, 0.1 wt% case.

